https://doi.org/10.5194/egusphere-2026-1599
Preprint. Discussion started: 4 May 2026

Spatially distributed water content thresholds for rainfall-induced landslide initiation

Juby Thomas[1], Rafael L. Bras[2], Leonardo V. Noto[3], Elisa Arnone[1]

[1]Polytechnic Department of Engineering and Architecture, University of Udine, Udine (UD), ITALY
[2]School of Civil and Environmental Engineering, Georgia Institute of Technology, Atlanta (GA), USA
[3]Dipartimento di Ingegneria, Università degli Studi di Palermo, Palermo (PA), ITALY

Correspondence to: Elisa Arnone (elisa.arnone@uniud.it)

Abstract. Rainfall-induced shallow landslides are among the most widespread natural hazards in mountainous regions, where intense precipitation, steep topography, and subsurface hydrological processes interact to trigger slope failures. Physically based approaches commonly derive rainfall-triggering thresholds using the framework proposed by Montgomery and Dietrich (1994), which defines instability conditions as a function of groundwater table position. However, this formulation neglects the stabilizing contribution of matric suction in unsaturated soils, potentially limiting its applicability. This study introduces a complementary metric, the Critical Soil Moisture (CSM), which, together with the classical Critical Wetness Index (CWI), provides a continuous hydro-mechanical description of stability across the full range of hillslope moisture states. The methodology is applied to the 28.6 km² Pontaiba basin in the Carnic Alps (northeastern Italy), a region characterized by steep terrain, high precipitation, and documented shallow landslides. Spatially distributed analyses based on topographic, soil, and landslide inventory data are combined with sensitivity analyses and an ensemble calibration procedure using Receiver Operating Characteristic (ROC) metrics to constrain uncertain parameters. Results delineate three stability regimes, unconditionally stable terrain, groundwater-controlled instability (CWI), and moisture-controlled instability (CSM), and identify slope-dependent hydrological thresholds that can support landslide early warning by focusing on state variables (groundwater, soil moisture) rather than rainfall alone.

1 Introduction

Rainfall-induced shallow landslides represent one of the most widespread and destructive natural hazards, causing thousands of fatalities and billions of dollars in economic losses each year (Emberson et al., 2020; Froude and Petley, 2018; Roman Quintero et al., 2025). These mass movements, typically mobilizing soil depths of 0.5 to 3.0 meters, are particularly prevalent in mountainous regions where steep terrain, weathered regolith, and intense precipitation events converge to create conditions conducive to slope failure (Van Asch et al., 1999; Guzzetti et al., 2008). Shallow landslides often occur rapidly in response to short-duration, high-intensity rainfall or prolonged wet periods that elevate pore-water pressures within hillslope materials (Iverson, 2000; Sidle and Bogaard, 2016). The coupling between hydrological forcing and mechanical response renders these

https://doi.org/10.5194/egusphere-2026-1599
Preprint. Discussion started: 4 May 2026

phenomena particularly sensitive to variations in precipitation patterns, soil moisture dynamics, and antecedent wetness (Bogaard and Greco, 2018; Ponziani et al., 2012). Given their widespread occurrence across diverse geomorphological and climatic settings, developing robust frameworks for identifying zones of heightened susceptibility and quantifying critical hydromechanical thresholds remains a paramount challenge in natural hazard research and risk management (Reichenbach et al., 2018; van Westen et al., 2006).

The frequency and magnitude of rainfall-induced landslides are fundamentally governed by hydrologic and meteorological controls that modulate subsurface moisture conditions and pore-pressure dynamics. The development of physically based slope stability models has provided a framework for translating hydrological forcing into mechanical response. The foundational work of Montgomery and Dietrich (1994) established the coupled hydrological-stability modeling paradigm, wherein hillslope stability is quantified through the Factor of Safety (FoS), the ratio of resisting to driving forces acting along potential failure planes. This framework integrates the infinite slope model (Taylor, 1948) with the Mohr-Coulomb failure criterion (Terzaghi, 1943; Terzaghi et al., 1996) to assess stability as a function of topographic attributes (slope angle, ω), soil mechanical properties, and hydrological state variables (groundwater table height above a failure plane). The elegance of this approach lies in its invertibility, i.e., for given geotechnical parameters and topography, critical hydrological conditions leading to failure can be identified by solving for the groundwater configuration that sets FoS to 1, its critical value (Montgomery and Dietrich, 1994). This inversion yields the Critical Wetness Index (CWI), defined as the ratio of the thickness of the groundwater table above the failure plane to the depth of the failure plane from the soil surface, which demarcates stable and unstable terrain as a function of ground slope angle. Subsequent implementations have demonstrated the utility of this framework across diverse hydrogeomorphic settings, enabling basin-scale hazard assessment through spatially distributed modeling of topographic and pedologic controls (Arnone et al., 2016; Baum et al., 2010; Brilli et al., 2025; Di Biagio et al., 2024; Dietrich et al., 1995; Wu and Sidle, 1995)

Despite their demonstrated utility, the critical thresholds derived from inverting the Montgomery and Dietrich (1994) slope stability model have a fundamental limitation, i.e., they are formulated exclusively for conditions where slope failure is triggered by positive pore-water pressures associated with a rising groundwater table (Arnone et al., 2011; Montgomery and Dietrich, 1994). In unsaturated soil zones above the water table, pore-water pressures are negative with respect to atmospheric pressure, generating matric suction that effectively increases shear strength by enhancing intergranular effective stress (Fredlund et al., 2012; Fredlund and Rahardjo, 1993; Lu and Likos, 2004). This additional cohesive strength, which varies as a function of soil moisture content by relating soil moisture to matric suction via the soil-water retention curve (SWRC), can provide substantial resistance to slope failure (Fredlund et al., 1996; van Genuchten, 1980; Lu and Godt, 2008; Vanapalli et al., 1996). Ignoring unsaturated zone mechanics therefore leads to systematic underestimation of stability in steep terrain and precludes identification of moisture-based failure thresholds in regions where groundwater tables may not reach critical depths. Several studies have incorporated unsaturated soil mechanics into slope stability analysis through extended Mohr-Coulomb criteria that include suction stress or matric suction contributions (Arnone et al., 2016, 2021; Bao et al., 1998; Bishop, 1955; Lepore et al., 2013; Öberg and Sällfors, 1997; Vanapalli et al., 1996).

https://doi.org/10.5194/egusphere-2026-1599
Preprint. Discussion started: 4 May 2026

The need for threshold-based hydromechanical stability demarcation stems from both scientific and operational imperatives. From a scientific perspective, a complete mechanistic understanding of rainfall-induced landslide triggering requires accounting of the full continuum of hydrological states, from dry conditions through unsaturated regimes to full saturation (Arnone et al., 2011; Lepore et al., 2013). A unified framework capable of identifying critical thresholds across this continuum enables systematic investigation of how soil type, topography, and rainfall characteristics interact to control landslide susceptibility. From an operational standpoint, threshold-based approaches provide actionable criteria for hazard assessment and early warning systems. Operational landslide early-warning systems increasingly rely on rainfall thresholds, hydrological indices, and real-time monitoring to anticipate failure conditions and issue alerts (Piciullo et al., 2018; Segoni et al., 2018b). However, most operational systems still depend on empirical rainfall thresholds that do not explicitly represent hydromechanical processes, limiting their ability to anticipate failures under evolving climatic and hydrological conditions (Guzzetti et al., 2020). Threshold-oriented frameworks that quantify critical moisture or groundwater states therefore have considerable potential for integration into next-generation early-warning systems, particularly under non-stationary climate forcing. To address these limitations, this study introduces a complementary metric called Critical Soil Moisture (CSM), extending the Montgomery-Dietrich approach by incorporating unsaturated soil mechanics via the extended Mohr–Coulomb criterion (Bishop, 1955) and the van Genuchten (1980) soil-water retention model. We implement this methodology in a case study in in the Carnic Alps of northeastern Italy. This location experiences one of the highest precipitation totals in the Alpine arc, exhibits pronounced morphological variability, hosts a well-documented inventory of shallow rainfall-induced landslides, and is projected to see increases in Alpine extreme precipitation as climate changes (Arnone et al., 2023, 2024; Estermann et al., 2025; Gobiet et al., 2014).

The objectives of this study are: (i) to formulate a unified hydro-mechanical framework capable of continuous stability assessment across saturated and unsaturated conditions; (ii) to calibrate and apply this approach at basin scale using available topographic, soil, and landslide inventory data; and finally (iii) validate, to the extent possible, the methodology.

2 Methodology

Factor of Safety (FoS) is used as a measure of the stability and is defined as the ratio of resisting to driving forces applied along the hillslopes, by accounting for gravity, soil resistance, and soil moisture dynamics within the terrain. When coupled with hydrological models, the most widely used FoS formulation is the one derived for the infinite slope model and grounded in the Mohr–Coulomb failure criterion (Montgomery and Dietrich, 1994; Terzaghi et al., 1996), which incorporates three distinct hydrostatic configurations defined by the position of a groundwater level relative to the potential failure plane: (1) a fully groundwater-submerged soil column, where the groundwater level extends continuously from the potential failure plane to the ground surface (Fig. 1a), in this configuration the soil column is fully saturated; (2) a completely groundwater-free condition, where no groundwater table exists above the potential failure plane, and the entire soil column contributing to shear resistance is devoid of groundwater (Fig. 1b); and (3) a partially groundwater-influenced profile, where the groundwater level

https://doi.org/10.5194/egusphere-2026-1599
Preprint. Discussion started: 4 May 2026

is located above the potential failure plane resulting in a saturated zone extending from the potential failure plane up to the groundwater level, with the remaining upper portion of the soil column dry (Fig. 1c). Under conditions a, b and c illustrated in Fig. 1, the equilibrium between resisting forces, gravity-driven forces, and positive pore pressures in saturated regions is described by the following equation (Arnone et al., 2011; Montgomery and Dietrich, 1994):

$$FoS = \frac{c}{\gamma_s z \sin\omega} - \frac{\gamma_w}{\gamma_s} \cdot \frac{h_w}{z} \cdot \frac{\tan\phi}{\sin\omega} + \frac{\tan\phi}{\tan\omega} \quad (1)$$

where c is the soil cohesion, ϕ is the angle of internal friction, γ_w unit weight of the water, ω is the slope of the soil column, γ_s is the unit weight of the water, z is the depth at which the FoS is computed and h_w is height of the water table with respect to the depth z. The term h_w/z identifies the Wetness Index (WI), defined as the ratio of height of the water table above the failure plane, h_w, to the depth of the soil column above the failure plane, z (Arnone et al., 2011; Montgomery and Dietrich, 1994).

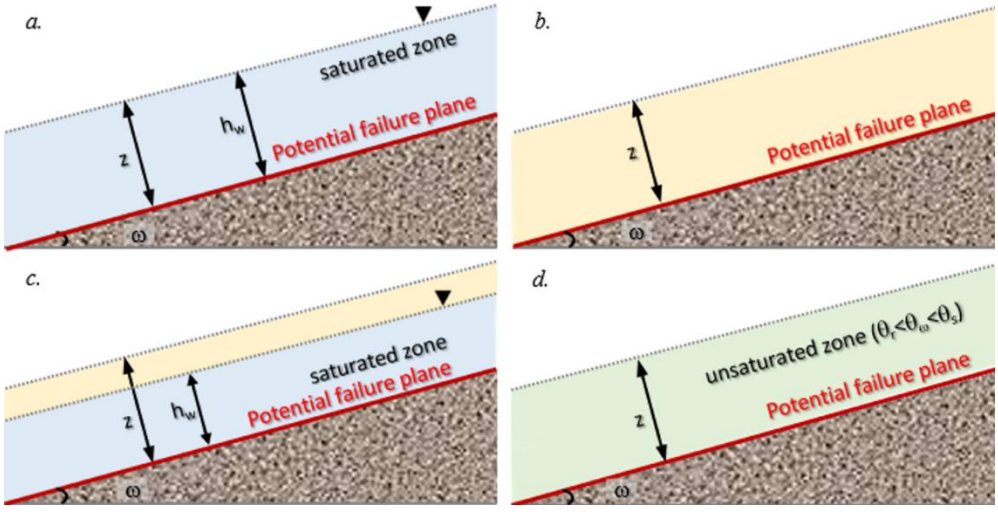

Figure 1: Schematic illustration of four possible hillslope conditions: (a) fully saturated soil column with the groundwater table at the surface; (b) dry condition with no groundwater table; (c) partially saturated condition with the groundwater table at a height h_w; and (d) condition where the groundwater table is absent, but soil moisture is present

As stated in Sect. 1, the limitation of the Montgomery and Dietrich formulation, Eq. (1), is that it is valid only for a failure plane within a saturated groundwater zone, or a completely dry situation. As will be shown below, that results in an underestimation of the steepest surface gradient below which a not fully saturated soil is stable. This underestimation is a consequence of assuming zero pore pressures in the "dry" zone when that region is apt to contain water, in an unsaturated state, resulting in negative pore-water pressures (matric suction) induced by capillary forces which in turn helps resist slope

https://doi.org/10.5194/egusphere-2026-1599
Preprint. Discussion started: 4 May 2026

failure. This omission results in an underestimation of shear strength in conditions where suction contributes significantly to slope stability and hence the possibility of steeper stable slopes.

To address the above limitation, this study incorporates the full spectrum of hydrological conditions governing slope stability by assessing the FoS under both groundwater-controlled conditions, characterized either by positive (Fig. 1a, c) or zero pore-water pressures (Fig. 1b); as well as conditions in which no groundwater table present above the potential failure plane, while the soil remains wet but unsaturated, and negative pore-water pressures (matric suction) contribute significantly to shear strength (Fig. 1d). The equation used to include this last condition is based on an extended failure criterion of Mohr–Coulomb, (Bishop, 1955), which utilizes the soil-water retention curve (SWRC) to find negative pore pressures in the unsaturated zones. The equation is (Bao et al., 1998; Fredlund et al., 1996; Khalili and Khabbaz, 2002; Öberg and Sällfors, 1997; Vanapalli et al., 1996):

$$FoS = \frac{c}{\gamma_s z \sin\omega} - \frac{\gamma_w}{\gamma_s} \cdot \frac{\psi_{(\theta)}}{z} \cdot \chi \cdot \frac{\tan\phi}{\sin\omega} + \frac{\tan\phi}{\tan\omega} \quad (2)$$

where $\psi_{(\theta)}$ is the negative pressure (or matric suction), which is related to soil moisture content θ by means the SWRC, and χ is a parameter that can be assumed equal to the effective saturation level (Lepore et al., 2013; Vanapalli and Fredlund, 2000):

$$\chi = \frac{\theta - \theta_r}{\theta_s - \theta_r} \quad (3)$$

where θ represents the soil moisture of the soil layer at the potential failure plane which is z meters down from the ground surface; θ_r and θ_s are the residual and the saturated soil moisture respectively. Using the van Genuchten, (1980) SWRC in Eq. (2), it results in:

$$FoS = \frac{c}{\gamma_s z \sin\omega} - \frac{\gamma_w}{\gamma_s} \cdot \frac{-\frac{1}{\alpha}\left[\left(\frac{\theta - \theta_r}{\theta_s - \theta_r}\right)^{-\frac{n}{n-1}} - 1\right]^{\frac{1}{n}}}{z} \cdot \frac{\theta - \theta_r}{\theta_s - \theta_r} \cdot \frac{\tan\phi}{\sin\omega} + \frac{\tan\phi}{\tan\omega} \quad (4)$$

where α is a scaling parameter related to the inverse of the air-entry suction and *n* is a dimensionless shape parameter of SWRC (van Genuchten, 1980).

Summarizing, if the failure plane lies within the saturated groundwater zone, Eq. (2) is limiting. If the failure plane lies within an unsaturated region, then Eq. (4) is limiting. Equations (1) and (4) converge at the extremes of complete dryness and complete saturation.

For a potential failure plane at depth z and a FoS equal to 1, both Eq. (1) and Eq. (4) can be inverted for a given surface slope angle, ω, and set of hydrological (θ_r, θ_s, n) and soil-mechanical properties (γ_s, c, and ϕ) to determine values of wetness index

https://doi.org/10.5194/egusphere-2026-1599
Preprint. Discussion started: 4 May 2026

or soil moisture at which failure occurs, allowing the delineation of stability regions of the terrain (Montgomery and Dietrich, 1994). Specifically, inversion of Eq. (1) determines the Critical Wetness Index (CWI) above which the soil column becomes unstable (Montgomery and Dietrich, 1994) for a failure plane within the saturated zone:

$$\mathrm{CWI} = \frac{h_w}{z} = \left(\frac{\tan\phi}{\tan\omega} + \frac{c}{\gamma_s z \sin\omega} - \mathrm{FoS}\right) \cdot \frac{\gamma_s}{\gamma_w} \cdot \frac{\sin\omega}{\tan\phi} \quad (5)$$

The upper half of Fig. 2 illustrates Eq. (5) (describing the conditions illustrated in Fig. 1a, b, and c) for a given set of parameters. The scale at the right gives the wetness index, the ratio of thickness of the saturation layer above the failure plane to depth to the failure plane. In these cases, the failure plane is always within the saturated zone. For angles less than ω* the soil is fully saturated, and the slope is always stable. For angles greater than ω**, occurring when the soil is dry above the failure plane, the slope is always unstable. In between ω* and ω** the groundwater level is above the failure plane but below the surface, the soil is not fully saturated. As can be seen the angle at which point the slope fails increases as the wetness index decreases, until a wetness index of zero and ω** are reached. Note that throughout this solution the pore pressure at the failure plane is always positive, never less than zero.

As mentioned previously, the problem with the above solution is that it does not consider a failure plane within a region where the soil is wet but not saturated, or unsaturated but not dry. In such conditions the matric potentials are negative, providing additional resistance to failure. That implies that stability can occur for slopes greater than ω** and soil saturation levels between $\theta = \theta_s$ (fully saturated) and $\theta = \theta_r$ (moisture content equal to a residual level, effectively completely dry). With the FoS equal to 1, Eq. (4) can be inverted to find an implicit relationship between the critical value of θ, named Critical Soil Moisture, CSM, and soil slope, ω:

$$1 = \frac{c}{\gamma_s z \sin\omega} - \frac{\gamma_w}{\gamma_s} \cdot \frac{-\frac{1}{\alpha}\left[\left(\frac{\mathrm{CSM}-\theta_r}{\theta_s-\theta_r}\right)^{-\frac{n}{n-1}} - 1\right]^{\frac{1}{n}}}{z} \cdot \frac{\mathrm{CSM}-\theta_r}{\theta_s-\theta_r} \cdot \frac{\tan\phi}{\sin\omega} + \frac{\tan\phi}{\tan\omega} \quad (6)$$

This is illustrated in the bottom half of Fig. 2. Note that the two solutions are continuous in terms of matric potential (negative) and soil pore pressure (positive), shown to the right of Fig. 2. The critical soil moistures corresponding to the matric potential are in the left axis of the bottom half of Fig. 2. Note that stability can be achieved for slopes greater than ω**.

In summary, in regions where the failure plane is within the saturated column, where ω*<ω<ω**, separation between stable and unstable areas is determined by the Critical Wetness Index, CWI (y axes on the right), which varies linearly with the slope, according to Eq. (5). Conversely, in regions where the failure plane is within unsaturated wet soils (negative pore pressures), where ω>ω**, separation between stable and unstable cases is defined in terms of the Critical Soil Moisture, CSM, which is highly nonlinear with slope, according to Eq. (6). Although two equations were employed to analyze hillslope stability, with respect to wetness index and soil moisture, the developed framework utilizing CWI and CSM provides a continuous

https://doi.org/10.5194/egusphere-2026-1599
Preprint. Discussion started: 4 May 2026

demarcation of the topography into stable and unstable from gentle to steep slopes. Notably, the CWI and CSM converge at the condition where the groundwater table is at the depth of failure surface and yet the soil remains saturated at that depth.

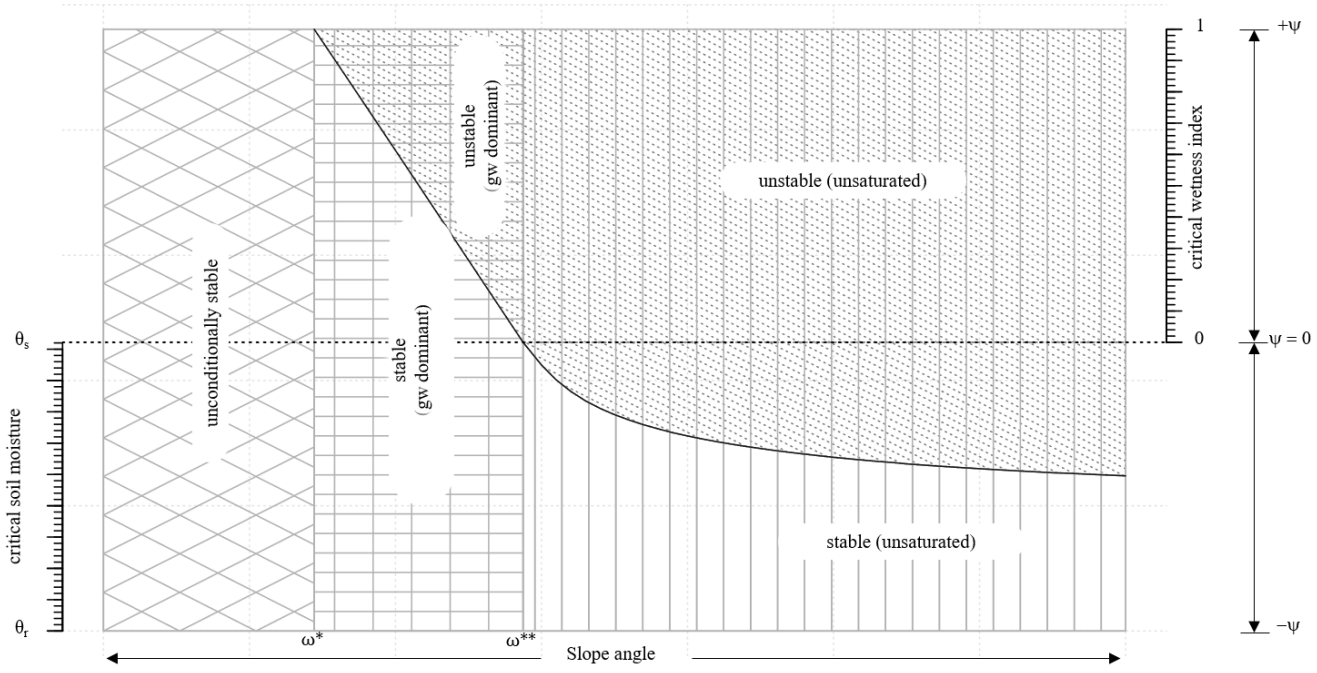

Figure 2: Summary of 3 stability regions and the CSM and CWI here defined, at a given hypothetical depth of failure surface (z), for given hydrological and mechanical parameters and for varying slope (x axis). Groundwater dominant (gw dominant) region are marked between ω* and ω.**

The ultimate objective is to use the conceptualization shown in Fig. 2 to classify regions over a basin that are prone to landsliding, or vice-versa. The classification would be a function of topography, i.e. surface gradient, and moisture state as represented by the CWI or the CSM. Limiting conditions would depend on the position of the failure plane, which is not known a-priori. Hence the analysis will seek to obtain the most probable stability classification given a distribution of possible failure planes. The overall methodological framework applicable at basin scale is described in Supplement S1.

3. Case study and datasets

3.1 Study area

The developed framework has been tested at a small basin called Pontaiba (28.62 km^2), which is a sub-basin of the major But basin (327 km^2), located in the Friuli Venezia Giulia region of Italy (Fig. 3).

https://doi.org/10.5194/egusphere-2026-1599
Preprint. Discussion started: 4 May 2026

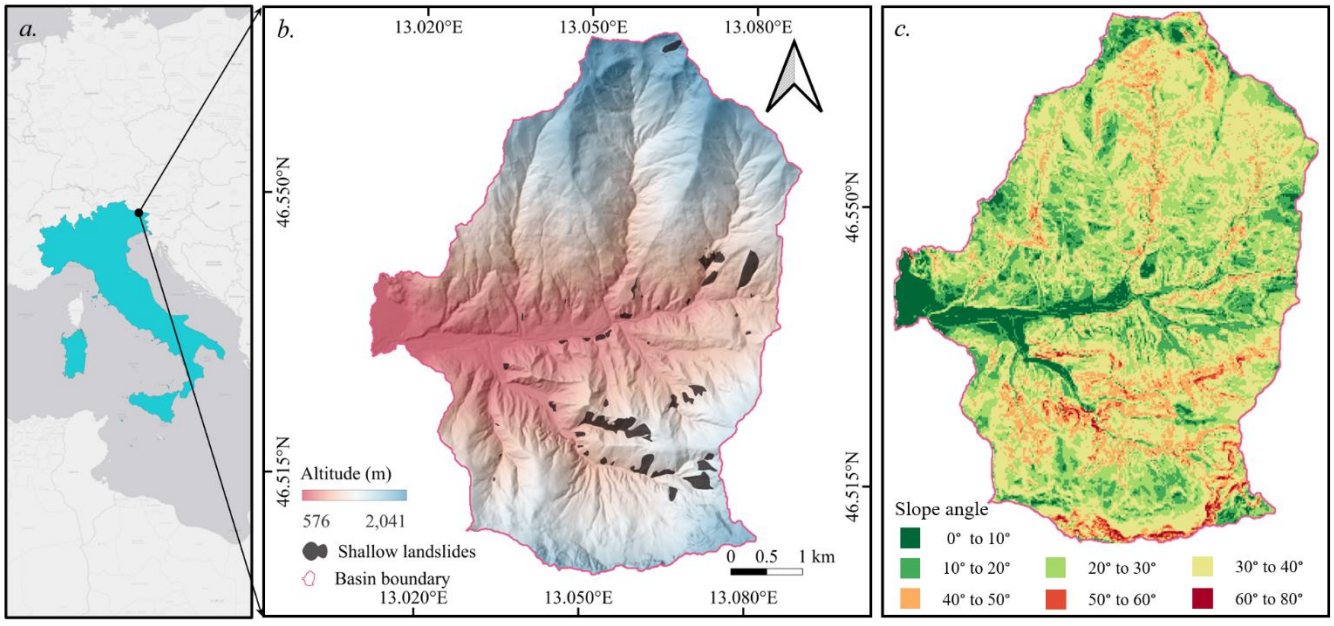

Figure 3: (a) Geographic location of the study area. (b) The selected basin, elevation, and documented rainfall induced shallow landslides, (c) slope classes with corresponding slope angles in degrees are shown.

The But River is the third most important tributary of the main Tagliamento river and extends across the eastern Italian Alps area known as Carnic Alps (Carnia). This area is identified as one of the wettest regions in the entire Alpine arc and receives mean annual rainfall between 2500 and 3500 mm (Fratianni and Acquaotta, 2017). The heavy precipitation is influenced by Mediterranean moisture sources and orographic uplift (Sodemann and Zubler, 2010). Heavy precipitation occurs between September and November, with a secondary maximum in spring (Ménégoz et al., 2020; Sodemann and Zubler, 2010). Additionally, the area is also characterized by snowfall typically from November to April. Land-surface processes and erosion induced by rainfall are significant in this part of the region (Arnone et al., 2023; Cucchiaro et al., 2024; Tarolli and Dalla Fontana, 2009). The selected Pontaiba basin is also known for being affected by rainfall triggered shallow landslides (Brunetti et al., 2025) as shown in Fig. 3b.

3.2 Topographic, land use and soil characterization

Topographic information of the basin is derived from a 10 m resolution Digital Terrain Model (DTM) provided by the Protezione Civile Regione Autonoma Friuli Venezia Giulia as a resampling of 1 m Lidar survey. The DTM was used to generate detailed slope distributions, capturing spatial variations in terrain steepness that directly affect gravitational driving stresses on hillslopes. The 10 m resolution provides a practical tradeoff between the need to capture essential local topographic variability without oversimplifying the terrain.

https://doi.org/10.5194/egusphere-2026-1599
Preprint. Discussion started: 4 May 2026

The analysis of the study area's topography revealed elevations ranging from 576 m to 2041 m (Fig. 3b), with a mean elevation of 1188 m. Derived slope values varied between 0.01° and 78.15° (Fig. 3c), with an average slope of 29.05°, indicating a predominantly steep terrain. The distribution of slopes highlights substantial local variability, which is critical for assessing geomorphological and hydrological processes.

Two widely used open-source databases from the Food and Agriculture Organization (FAO) are used to characterize the soil: SoilGrids (Hengl et al., 2017) and the Harmonized World Soil Database v2.0, HWSD v2 (FAO, 2023). SoilGrids provides gridded estimates (~250 m resolution) of USDA soil texture classes. Within the study basin, SoilGrids indicated two dominant soil classes, loam and clay loam. In contrast, HWSD uniformly classified the basin as loam. To reconcile these differences, average values of sand, silt, and clay fractions were computed for the SoilGrids-derived loam and clay loam units and projected onto the USDA soil texture triangle. Notably, the mean composition of the "clay loam" pixels plotted near the "loam" field, suggesting that a uniform loam designation is an acceptable simplification for the basin. Consequently, a single representative loam texture was adopted for the subsequent hydro-mechanical characterization. For the given soil type, the hydrological characterization of the parameters is carried out using the pedotransfer functions implemented in ROSETTA software (Schaap et al., 2001, 2004; Zhang and Schaap, 2017).

Mechanical parameters not directly available from the global datasets, specifically soil cohesion and internal friction angle, were initially assigned based on values reported in a previous study (Del Fabbro et al., 2024) for a geologically and pedologically similar basin in the same region. While fields and laboratory tests have demonstrated quite stable and high values of friction angles, the values of soil cohesion are more uncertain. For this reason, we carried out a sensitivity analyses and a calibration procedure to assess the most reliable values of soil cohesion, as explained later. A complete summary of the applied hydraulic and mechanical parameter values is provided in Table 1.

Table 1 Hydrologic and mechanical parameters for the selected basin. The unit weight of the soil is considered uniform from the potential failure plane to the ground surface. Hydrological properties are derived based on the soil map and mechanical properties are derived from previous studies. Source: Rosetta Database (USDA class averages).

Parameter	Symbol	Selected value
Soil friction angle	(ϕ)	30°
Unit weight of water	γ_w	9816 Nm^{-3}
Unit weight of soil	γ_s	16687.2 Nm^{-3}
Residual water content	θ_r	0.0270
Saturated water content	θ_s	0.4610
van Genuchten SWRC parameter	α	0.036 cm^{-1}
van Genuchten SWRC parameter	n	1.56

https://doi.org/10.5194/egusphere-2026-1599
Preprint. Discussion started: 4 May 2026

3.3 Landslide inventory

Evidence of the occurrence of shallow landslides in the past were verified thorough two national archives, the *Inventario dei Fenomeni Franosi in Italia*, IFFI, (Trigila et al., 2026) curated and publicly disseminated by the Italian Institute for Environmental Protection and Research (*Istituto Superiore per la Protezione e la Ricerca Ambientale*, ISPRA); and the *ITAlian rainfall-induced LandslIdes Catalogue*, ITALICA (Peruccacci et al., 2023). The ISPRA-IFFI database compiles georeferenced records of mass movements across Italy using historical reports, aerial photointerpretation, field surveys, and Regional Environmental Protection Agencies reports (Agenzia Regionale per la Protezione Ambientale, ARPA).

Figure 3 shows the shallow rainfall-induced landslides for the Pontaiba area, selected from the ISPRA–IFFI inventory. The events cover a total area of 0.63 km^2 (2.21% of the basin), for a total of 48 polygons. The average area is 13,150.35 m^2, with a minimum of 307.05 m^2 and maximum of 14,1260.8 m^2. For the selected events, there is no information on the time the landslides occurred. Additionally, the ISPRA-IFFI does not include standardized measurements on depth to failure plane or slip surface. Qualitative field surveys were conducted within the study basin to verify the spatial accuracy and geomorphic characteristics of inventoried landslides.

3.4 Sensitivity analysis

If the depth of failure were available from the landslide inventory, and all physical parameters known, then the solution in Fig. 2 would provide the CWI or the CSM at which the failure occurred, given the topographic slope at the failure point. The reasonableness of those estimates could be an indirect verification of the model; but since the failure depth is not known and parameters are uncertain, the verification of model behaviour must be done probabilistically. The idea is to find the most probable points of instability in the region and check if they are consistent with the observed areas of failure.

A sensitivity analysis was carried out to assess the method's sensitivity to the two parameters for which data were unavailable: failure depth and cohesion. The analysis was first performed with respect to failure depth by fixing the cohesion at 9,000 Pa. The response of the basin at six different failure depths, z, of 0.50 m, 0.75 m, 1.00 m, 1.25 m, 1.50 m, and 2.00 m was obtained. Subsequently, cohesion was varied from 5,000 Pa to 15,000 Pa at a step of 2,500 Pa, while maintaining a constant depth to the failure plane to evaluate its influence on model response.

https://doi.org/10.5194/egusphere-2026-1599
Preprint. Discussion started: 4 May 2026

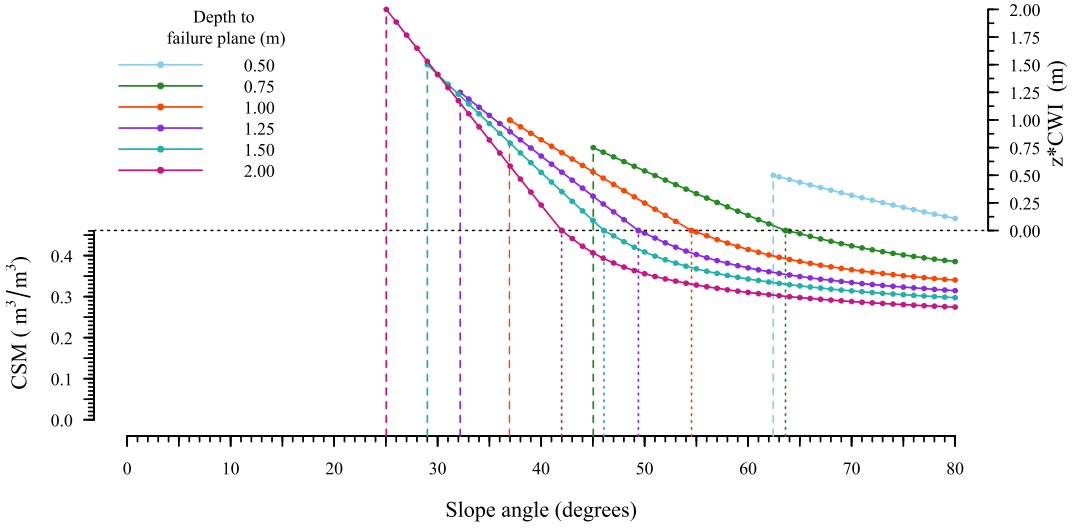

Figure 4: Behaviour of the selected terrain at six potential failure planes of 0.50 m, 0.75 m, 1.00 m, 1.25 m, 1.50 m, and 2.00 m down with fixed hydro-mechanical parameters reported in Table 1, for c = 9,000 Pa. Critical Wetness Index (CWI) multiplied by selected depth (z) and Critical Soil Moisture (CSM) are plotted along the y-axis and slope angle is shown along x-axis. Dashed lines indicate the ω* and dotted lines indicate the ω corresponding to selected depths.**

Figure 4 presents the analysis for the application of the general framework to the study area (Fig. 3), using the hydro-mechanical parameters listed in Table 1 and cohesion equal to 9,000 Pa, for the six fixed depths. To enhance clarity and emphasize depth-dependent behaviour, Fig. 4 presents the CWI multiplied by z ($CWI \times z$), acknowledging that this product represents the critical value of groundwater table depth above the selected failure plane, h_w, in Eq. (5). The x-axis represents slope angle in degrees, ranging from 0° to 80° which are the minimum and the maximum slope observed in the basin.

For a 2.00 m depth to potential failure plane, ω** = 41.98° (Fig. 4), marks the transition between groundwater-driven and soil-moisture-driven instability regimes. Below this threshold, slope stability is governed by the dynamics of the total saturated soil thickness above the potential failure surface, here described in terms of $CWI \times z$ (top portion of Fig. 4). Beyond ω**, the y-axis switches to CSM (bottom portion of Fig. 4, Eq. (6), reflecting instability controlled by unsaturated soil moisture conditions.

https://doi.org/10.5194/egusphere-2026-1599
Preprint. Discussion started: 4 May 2026

Table 2 Depth-wise change in critical slope angles, ω* and ω, and percentage area of unconditionally stable, conditionally stable in terms of CWI, conditionally stable in terms of CSM. The total area of the basin is 28.62 km^2.**

Depth (m)	Slope ω* (°)	Slope ω** (°)	Unconditionally stable (%)	Conditionally stable - CWI (%)	Conditionally stable - CSM (%)
0.50	62.43	86.14	98.66	00.23	0.00
0.75	45.04	63.61	94.52	04.20	0.20
1.00	36.95	54.53	77.13	20.88	0.90
1.25	32.18	49.40	57.01	39.85	2.00
1.50	29.01	46.07	44.38	50.89	3.60
2.00	25.04	41.98	31.30	59.68	7.90

Table 2 provides the percentage of the basin area in each of the stability regimes for each failure depth assumption. Throughout this analysis, the hydro-mechanical properties in Table 1 (including cohesion) are held constant in order to isolate the influence of the assumed depth to the potential failure plane (z) on stability regimes. Across the basin, 31.30% of the area between 0° to 25.04° (ω*) is identified as 'unconditionally stable' when the depth to potential failure plane is 2.00 m, with the hydro-mechanical properties from Table 1. The region between 25.04° (ω*) and 41.98° (ω**), which is 59.68% of the basin, is labelled as 'conditionally stable' and a failure will occur only when there is an explicit presence of groundwater table above the potential failure plane which is 2.00 m down. This means that the potential failure at 2.00 m is controlled by the thickness of the total saturated depth, h_w, above the potential failure plane. As the slope increases from 25.04°, less saturated soil depth, i.e., $CWI \times z$, is required to initiate a failure, and at 41.98°, theoretically total saturation is required only at the failure surface layer. The region steeper than 41.98° which is 7.90% of the basin (Table 2) is again termed as 'conditionally stable' with the stability defined in terms of CSM. As shown in Figure 4, at 41.98°, the y-axis switches from CWI to CSM, starting with a CSM of 0.46, which is the saturated water content corresponding to loam type soil (Table 1). Terrain with gentler slope angles up to ω* remains invariably stable regardless of the soil water content. In this region neither groundwater nor soil moisture contributes to failure. Clearly, this result is valid only within the assumptions of the implemented model.

The $CWI \times z$ curve from 25.04° to 41.98° shows a linear steep negative gradient, indicating how less groundwater depth above the failure plane is needed to destabilize steeper slopes. The CSM curve starts at 0.46, corresponding to the saturated water content of loam, from 41.98° onwards. The transition from $CWI \times z$ to CSM marks a hydro-mechanical behavioural shift, from groundwater pressure-driven instability to soil moisture suction-driven instability. The CSM curve (above 41.98°) initially follows a highly non-linear steep decline (between 41.98° and 65°), then plateaus at very high slopes (above 65°), suggesting that; (i) beyond a certain steepness, gravity becomes the dominant destabilizing force, and even minimal moisture contributes to instability, and (ii) the plateau implies reduced influence of soil suction forces at steeper terrains. Because the infinite-slope framework assumes a planar, laterally extensive geometry and moderate slope angles, its predictions at very steep slopes should

https://doi.org/10.5194/egusphere-2026-1599
Preprint. Discussion started: 4 May 2026

be interpreted with caution. This is consistent with reports of non-physical behaviour in the classical formulation at $\omega \gtrsim 45°–50°$, as well as the development of revised variants of the framework (Tsai and Yang, 2006).

As we move to a shallower z of 1.50 m, the terrain remains unconditionally stable for slope angles up to 29.01° (ω*). The unconditionally stable area is 44.38% larger than the previous case (Table 2). Between 29.01° and 46.07° (ω**), stability is controlled by the CWI (50.89% of the basin). The conditionally stable area that is governed by the unsaturated soil moisture conditions reduces to 3.60% and corresponds to regions steeper than 46.07°. A similar stability regime pattern is observed for the shallower failure plane at 1.25 m. Here, 49.40% of the basin at a slope less than 32.18° (ω*) is classified as unconditionally stable. Stability in the interval between 32.18° and 49.40° is controlled by groundwater conditions (CWI×z). Slopes exceeding 49.4° fall under the control of the soil moisture (2.00% of the basin). The same trends are observed as the depth to failure plane become shallower: 1.00 m, 0.75 m, and 0.50 m. The relatively high friction angle and cohesion assumed in this application increase the shear resistance of the soil mass which, together with the reduced gravitational driving stress at z = 0.50 m, allows even steeper slopes to remain stable. As z decreases, the ω* and ω** shift towards steeper angles and more areas eventually become unconditionally stable.

As previously mentioned, the extent of unconditionally stable terrain, as well as the computed values of CWI and CSM, are significantly influenced by variations in cohesion, *c* in Eq. (4) and (5). To evaluate the sensitivity of the modeling framework to cohesion variability, a systematic analysis was conducted across the selected basin using discrete cohesion values while maintaining uniform friction angle (φ) and invariant soil properties as specified in Table 1.

Figure 5 shows the spatial distribution of unconditionally stable areas and CWI and CSM across the basin obtained for cohesion values equal to 5,000, 7500, 10,000, 12,500 and 15,000 Pa respectively, across the previously selected depths of potential failure plane (z). The union of shades of green and red areas denotes the conditionally stable region. The spatial distribution of conditionally stable areas and critical water content thresholds is strongly influenced by basin morphology, particularly the slope distribution. In fact, consistently with trends observed in Table 2, at shallower failure depths, the basin predominantly exhibits unconditionally stable behavior across a wide range of slope angles. However, as the depth to the potential failure plane (z) increases, a progressive reduction in unconditionally stable areas is noted. Shallow failure depths require the presence of a groundwater table above the failure plane (i.e., saturated conditions) to initiate failure, whereas deeper regions become increasingly susceptible to failure under unsaturated conditions, governed by lower CSM thresholds. This trend is accompanied by a transition from CWI to moisture-controlled instability, particularly in the steepest regions of the basin. At greater depths (e.g., 1.50 m and 2.00 m), steeper slopes require relatively lower moisture content (i.e., lower CSM thresholds) to reach failure. The observed decline in CSM thresholds with increasing depth and slope angle highlights the coupling between topographic parameters and hydro-mechanical forces.

https://doi.org/10.5194/egusphere-2026-1599
Preprint. Discussion started: 4 May 2026

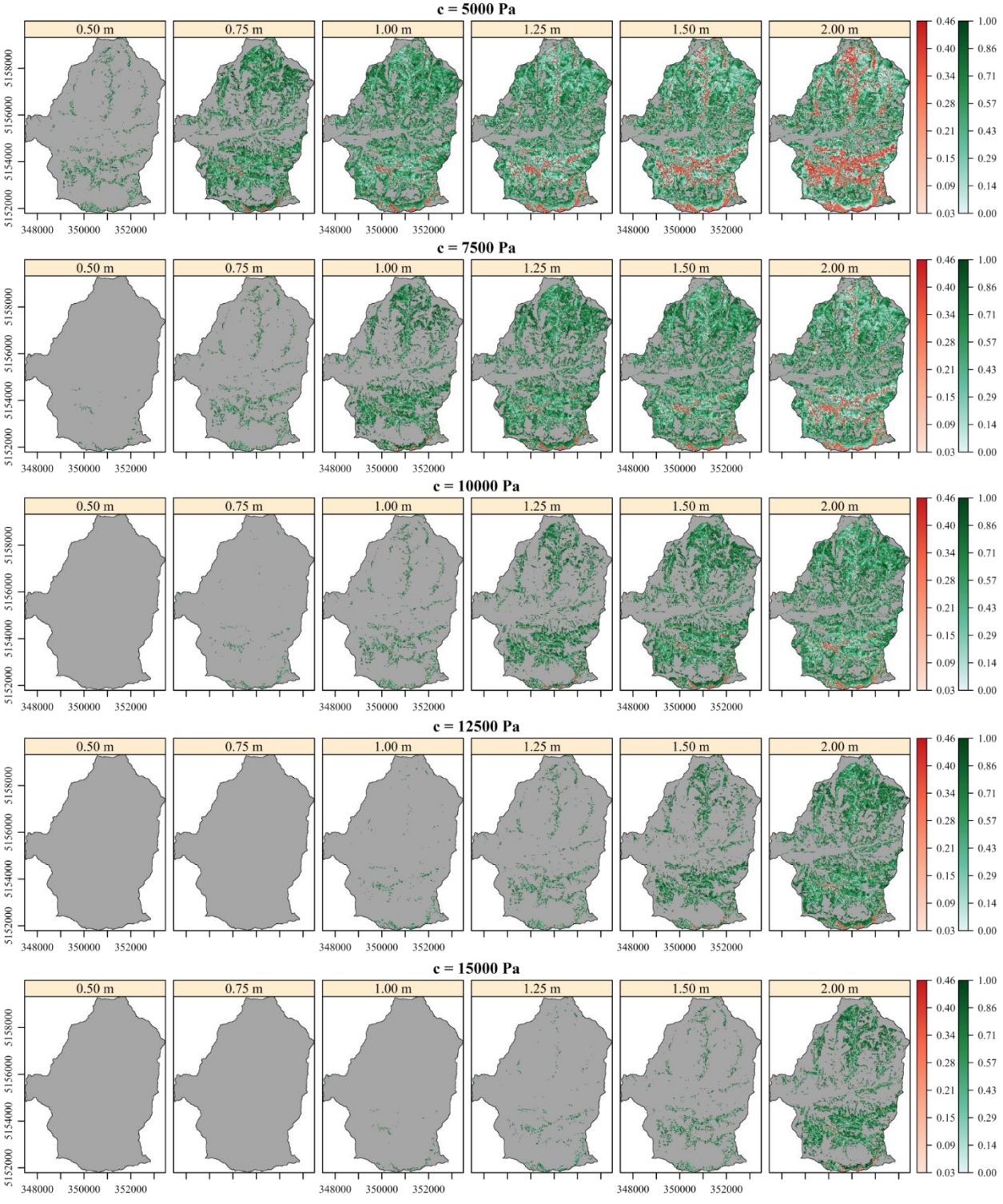

https://doi.org/10.5194/egusphere-2026-1599
Preprint. Discussion started: 4 May 2026

Figure 5: Maps of Critical Soil Moisture (CSM) and Critical Wetness Index (CWI) for varying depths of potential failure planes (z) and soil cohesion (c).

Increasing cohesion results in the extension of unconditionally stable zones into relatively deeper soil layers and in a pattern of conditionally stable areas following the steepest areas, even along the stream embankment, while reductions in cohesion causes potential failures even at shallow depths. Figure 6 shows a visual representation of variation in the percentage of terrain classified as unconditionally stable, conditionally stable but susceptible to failure under saturated conditions, and conditionally stable but susceptible to failure even under unsaturated conditions, across different cohesion values (c) and depth to the potential failure plane (z).

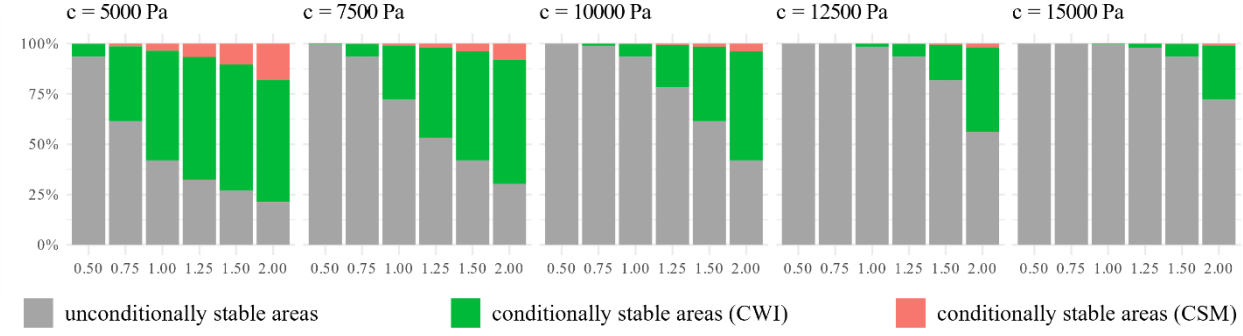

Figure 6: Variation in the percentage of terrain classified as unconditionally stable, conditionally stable but susceptible to failure under saturated conditions, and conditionally stable but susceptible to failure even under unsaturated conditions, across different cohesion values (c) and depths to the potential failure planes (z). Depth (in meters) is shown along the x-axis of each panel corresponding to the selected cohesion.

3.5 Model calibration procedure

The lack of explicit information on failure depths, prevented the use of a conventional calibration and validation approach. Based on field observations and sensitivity analyses (Sec. **Errore. L'origine riferimento non è stata trovata.**), soil cohesion and depth to potential failure plane are the most uncertain and influential variables governing the model performance. Accordingly, calibration with a given landslide inventory focused on identifying the most plausible combinations of the two variables that reasonably reproduce the observations. We adopted a repeated random sampling procedure that inverts traditional performance indices to identify the most reliable parameter set. The metrics used are the Receiver Operating Characteristic (ROC) curve and its associated metrics, e.g., the area under the ROC and the Youden's J index (Youden, 1950). Details of the performance metrics used for the calibration procedure are provided in Supplement S2.

The reference landslide inventory is rasterized to match the spatial resolution of the basin-level CWI and CSM maps, which inherit the 10 m resolution of the DEM used in their derivation. The CWI and CSM outputs are then converted into binary

https://doi.org/10.5194/egusphere-2026-1599
Preprint. Discussion started: 4 May 2026

classes representing landslide and non-landslide conditions. To adopt a conservative classification approach, all conditionally stable areas are categorized as landslides, as they indicate zones with the potential to fail if the corresponding CWI or CSM thresholds are exceeded. Since failure depth is also an unknown, we generated the ROC and the Youden's J index for repeated realizations of possible failure depths, referring to a pre-described distribution of failure depths.

We opted to use distributions of representative depth values from inventories of shallow rainfall-induced landslides in similar geomorphic settings, confirmed with visits to landslide locations at the site (Fig. 7). Knowledge of the area favoured intermediate failure depth and excluded very shallow and deep landslides. This is consistent with from rainfall-induced shallow landslide events reported in a similar steep, vegetated and rainy site Puerto Rico, where shallow landslides were predominantly mobilized within the 1.0 to 1.5 m range (Ramos-Scharrón et al., 2022).

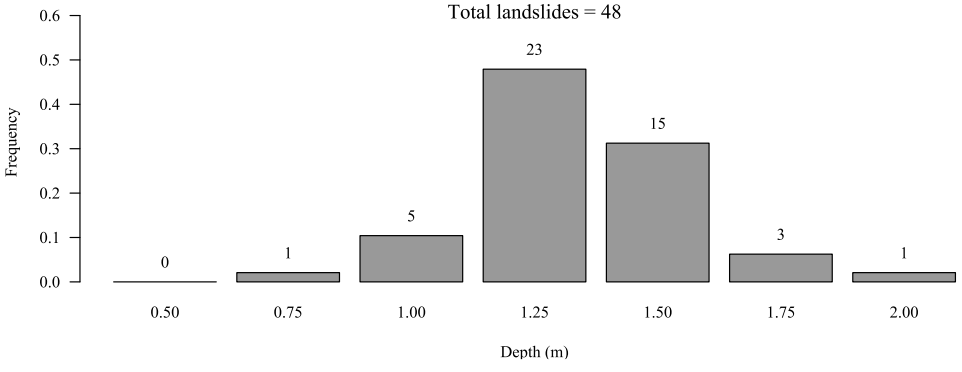

Figure 7: Frequency distribution of assigned depths to failure plane used in the probabilistic depth assignment procedure, highlighting the emphasis on mid-range depths (with a peak at 1.25 m).

Summarizing the calibration procedure comprised of the following steps:

i. Soil cohesion is treated as the threshold parameter governing classification of terrain into unconditionally stable areas (no-landslide) and conditionally stable areas (landslide-prone).

ii. 500 synthetic spatial distributions of failure depths (FD scenarios) are generated and assigned to observed landslides. Each FD scenario is created by randomly sampling from a discretized set of representative failure depths (0.50 to 2.00 m in 0.25 m increments) according to a predefined frequency distribution (Fig. 7).

iii. For a given set of assigned failure depths, cohesion is systematically varied between 0 and 35,000 Pa, testing over the full range of plausible soil strengths, from cohesionless conditions (0 Pa) to highly cohesive soils (35,000 Pa) in increments of 200 Pa. For each FD scenario ROC curves, and Youden's J indices are derived to quantify model

https://doi.org/10.5194/egusphere-2026-1599
Preprint. Discussion started: 4 May 2026

performance. It implies that for each ROC curve there is a number of Youden's J indices equal to the number of cohesion values used to generate the ROC curve;

iv. For each FD scenario, cohesion yielding the maximum Youden's J statistic is retained as the most reliable calibration outcome, identifying the cutoff cohesion value that best discriminates between stable and unstable terrain.

5. Results

The subsequent analysis describes the results of the modelling framework obtained for the ROC-based calibration procedure of soil cohesion.

Figure 8 presents the ensemble of 500 ROC curves generated by repeatedly applying the probabilistic depth assignment procedure described in Sect. 3.5 (FD scenarios). The ROC curves plot the rate of true positives or "sensitivity" (identifying a landslide where one is found) versus one minus "specificity". Specificity is the true negative rate, identifying a non-landslide location where there is none. One minus specificity is then the False Positive rate (see Supplement S2 for details). A random identification will have a ROC curve as a 45° straight line. A perfect prediction would have a sensitivity and specificity equal to 1, implying a False Positive rate of 0. Each curve corresponds to a unique realization of synthetic landslide depth data, created by randomly assigning depths to potential failure plane based on the defined frequency distribution reported in Fig. 7. Among the 500 ROC curves, that characterized by the highest Youden's J index (sum of sensitivity plus specificity minus 1) is chosen to identify the optimal model realization. Highest Youden index is the farthest possible event from complete randomness. The best cohesion values are chosen by the simulation with highest Youden's J index.

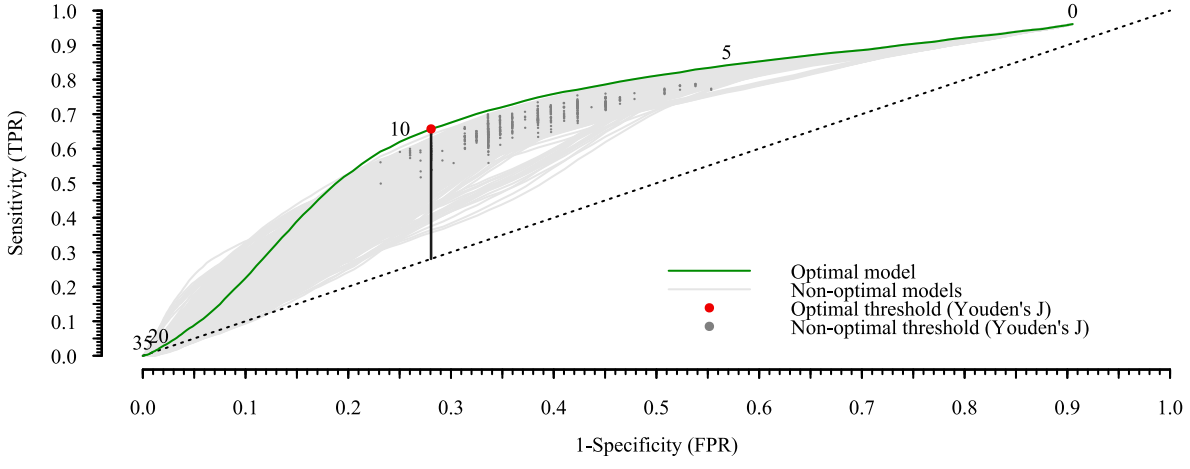

Figure 8: Receiver Operating Characteristic (ROC) curve ensemble from 500 iterations. Each curve represents a different randomized depth realization according to distribution in Fig. 7. The green curve indicates optimal model performance, and the red

https://doi.org/10.5194/egusphere-2026-1599
Preprint. Discussion started: 4 May 2026

marker on this curve corresponds to the highest Youden's J index. The gray curves indicate the non-optimal models and markers on these curves indicate the best Youden's J parameter for that corresponding model. Cohesions along the optimal ROC curve are indicated in the range of 0 to 35,000 Pa.

The gray curves show the distribution of ROC curves from all non-optimal model runs. The dotted diagonal line represents the performance of a random classifier, and all the model curves are correctly positioned above this line, indicating that the model has robust predictive power. The green curve represents the model with highest Youden's J index. This curve sits closest to the top-left corner of the plot, indicating a superior balance between Sensitivity and Specificity. The red marker on the green curve indicates the points where the maximum Youden's J index is achieved, equal to 0.37. This point represents the best compromise between correctly identifying landslides (high sensitivity) and correctly identifying stable areas (high specificity), thus defining, for a fixed FD scenario, the optimum value for the discriminating threshold, which in this case is soil cohesion. Specifically, the optimum cohesion that provides the highest performance is equal to 9,400 Pa. The spread in ROC curves reflects uncertainty introduced by cohesion and depth variability. The many gray dots represent the individual Youden's J values for the non-optimal models, showing the distribution of performance.

Figure 9 illustrates the maximum Youden's J statistics obtained from each of 500 individual ROC curves alongside the soil cohesion values that produced these respective maxima. The red point identifies the global maximum Youden's J value of 0.38, occurring at a cohesion of 9,400 Pa, the gray shaded band bounded by vertical dotted lines highlights the 95% confidence interval for optimal cohesion values, spanning from roughly 5,800 Pa to 9,600 Pa with a median of 8,000 Pa. This suggests a relatively narrow range of cohesion values consistently yielding good model performance across the 500 ROC curve iterations in spite of the initially selected cohesion range (0 – 35,000 Pa).

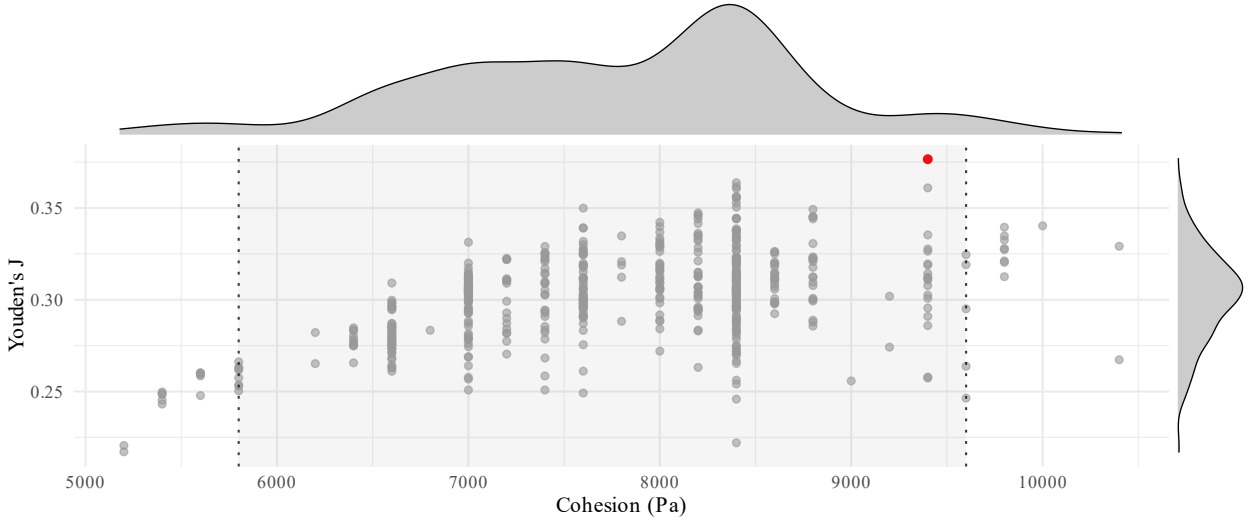

https://doi.org/10.5194/egusphere-2026-1599
Preprint. Discussion started: 4 May 2026

Figure 9: Maximum Youden's J statistics from individual ROC curves and their corresponding optimal cohesion values. The red point indicates the cohesion value (9,400 Pa) yielding the maximum Youden's J (0.38). Shaded area and dotted lines show the 95% confidence interval (5,800 Pa to 9,600 Pa). Marginal densities depict distributions of cohesion (top) and Youden's J (right).

The cohesion distribution suggests that higher cohesion values consistently exhibit better predictive power under the applied hydro-mechanical framework. Meanwhile, the Youden's J density confirms that many model realizations attain performance close to the global maximum, indicating stable and reliable model calibration despite uncertainties. The observed spread in optimal cohesion values among realizations primarily reflects the uncertainty associated to the depth to the failure plane, z, due to the lack of depth information associated with the documented landslides in the study area. An alternative to using the maximum Youden J value to select the best cohesion is to pick the most probable cohesion value. From Fig. 9 that would be 8,400 Pa with a similar Youden's index.

Figure 10 illustrates the spatial distribution of CSM and CWI across the study area for six potential failure plane depths, utilizing the optimized cohesion parameter of 9,400 Pa. The depth-dependent analysis reveals a systematic transition from predominantly stable to increasingly susceptible terrain.

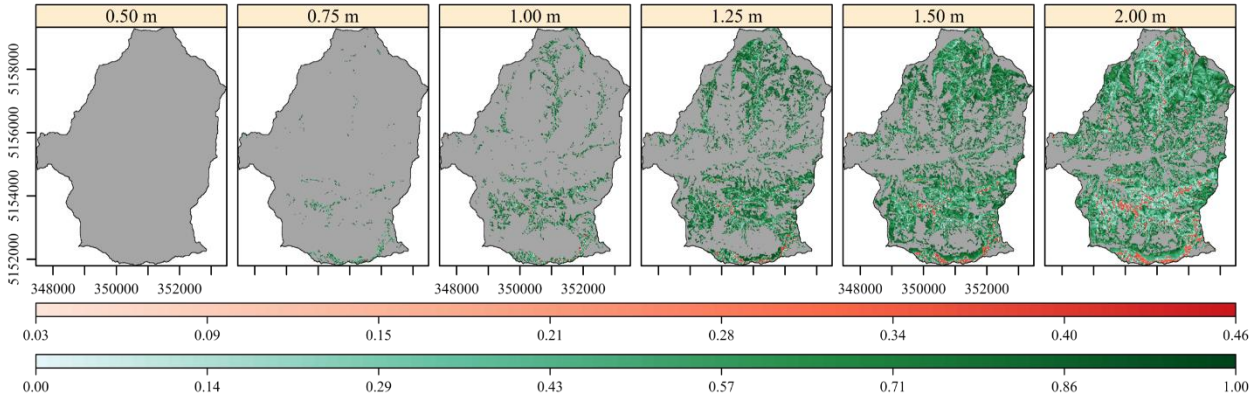

Figure 10: Spatial distribution of Critical Soil Moisture (CSM) and Critical Wetness Index (CWI) for varying depths of potential failure planes (z), based on the optimum cohesion of 9,400 Pa. Shades of red indicate regions where slope instability is governed by unsaturated soil moisture conditions (CSM), while shades of green correspond to regions where failure is controlled by the relative position of the groundwater table (CWI). Gray areas denote the unconditionally stable terrain at the respective depth to potential failure plane.

At the shallow failure depth of 0.5 m, the study area exhibits complete unconditional stability (Fig. 10Figure 10 and Table 3), demonstrating that gravitational driving forces are insufficient to overcome soil shear strength under any hydrological scenario. This represents one extreme of the stability spectrum, where topographic and material constraints preclude failure initiation. Conversely, at z = 2.0 m, the terrain shows pronounced susceptibility to hydrological triggering, with only 38.84% remaining unconditionally stable. The majority of the catchment (61.16%) transitions to conditional stability, predominantly controlled by groundwater fluctuations (56.49% CWI-controlled) with a notable fraction (4.67%) susceptible to failure under unsaturated conditions (CSM-controlled). This configuration represents the opposite extreme, where extensive areas become vulnerable to

https://doi.org/10.5194/egusphere-2026-1599
Preprint. Discussion started: 4 May 2026

moisture-induced instability. The intermediate depth scenario at z = 1.25 m provides the most realistic representation of natural slope stability conditions, with 72.35% unconditionally stable terrain and 27.65% exhibiting conditional stability. This configuration shows a balanced distribution between stable hillslopes and hydrologically-sensitive areas, predominantly controlled by groundwater dynamics (26.68% CWI-controlled) with minimal unsaturated zone influence (0.98% CSM-controlled).

It is critical to emphasize that the depicted CSM and CWI values represent threshold conditions for potential instability rather than immediate failure indicators. Areas displayed in shades of red or green colours denote zones that would become unstable upon reaching the specified moisture or groundwater conditions. Thus, these regions identify zones of heightened landslide hazard under changing hydrological conditions rather than forecasting instantaneous failure.

Table 3: Proportion of terrain classified into stability regimes across varying depths to the potential failure plane (z), based on the optimal cohesion of 9400 Pa. Conditionally stable areas are further partitioned into those governed by the Critical Wetness Index (CWI) and those governed by Critical Soil Moisture (CSM).

Depth (m)	Unconditionally stable (%)	Conditionally stable (%)	Conditionally stable - CWI (%)	Conditionally stable - CSM (%)
0.50	100	0	0	0
0.75	98.41	1.59	1.58	0.01
1.00	90.64	9.36	9.02	0.34
1.25	72.35	27.65	26.68	0.98
1.50	56.44	43.56	41.65	1.91
2.00	38.84	61.16	56.49	4.67

To produce an operationally interpretable instability map with the found cohesion value (c = 9,400 Pa), the failure depth is fixed at z = 1.25 m, corresponding to the modal class of the empirical frequency distribution (Fig. 7). This depth is selected as it represents the most frequently observed failure configuration in comparable terrain while avoiding the stability overestimation associated with shallower planes (z < 1.0 m) and the excessive susceptibility predicted at greater depths (z > 1.5 m; Table 3). The resulting CWI and CSM thresholds are shown in Fig. 11. The spatial distribution (Fig. 11a) reveals a clear morphological control, with CWI-controlled terrain concentrated along steeper mid-slope sectors and valley flanks, CSM-controlled areas confined to the steepest slopes, and unconditionally stable terrain occupying low-gradient zones, consistent with Table 3. The strong overlap between CWI-controlled regions and observed landslides (Fig. 3b) indicates a robust correspondence between predicted instability and failure locations. This is further supported by the slope-based analysis (Fig. 11b), where landslide occurrence frequency rises sharply beyond an approximate slope angle of 32°, peaks within the CWI-controlled slope range, and extends into the CSM-controlled domain up to approximately 65°, before declining at the steepest

https://doi.org/10.5194/egusphere-2026-1599
Preprint. Discussion started: 4 May 2026

gradients. This distribution indicates that while groundwater-driven instability governs the majority of documented failures, a non-negligible proportion of landslides occur under unsaturated conditions on very steep terrain, consistent with the dual-threshold framework proposed in this study. However, it is worth to observe that in some of the very steep and red areas, which are CSM-controlled and where no landslides are observed, the critical thresholds are unlikely reached at the selected depth.

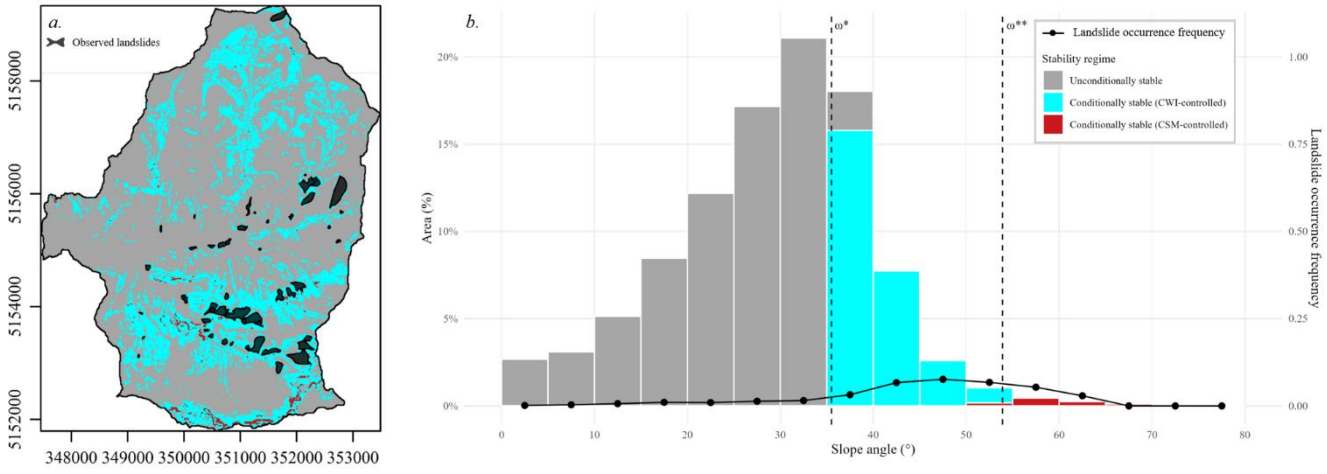

Figure 11: Instability classification for c = 9,400 Pa and the representative failure depth, z = 1.25 m. (a) Spatial distribution of: unconditionally stable (gray), groundwater-controlled conditionally stable (CWI-governed; cyan), and moisture-controlled conditionally stable (CSM-governed; red) stability regions. Documented shallow landslide polygons from the ISPRA–IFFI inventory are superimposed as black outlines. (b) Distribution of slope angles across stability classes. Stacked bars indicate the number of 10 m grid cells within each 5° slope interval, color-coded by stability regime. The black line denotes landslide occurrence frequency per slope bin. Vertical dashed lines indicate the critical slope angles ω* and ω delineating transitions between unconditionally stable, CWI-controlled, and CSM-controlled regimes, respectively.**

5 Discussion and conclusions

The development of physically based hydrological response thresholds through the spatially distributed CWI and CSM framework represents a significant step toward more mechanistic and adaptable landslide hazard assessment. By explicitly incorporating unsaturated soil mechanics into the classical Montgomery-Dietrich (1994) stability formulation, this study addresses a fundamental limitation of physically based models that typically consider instability only after the development of positive pore-water pressures. Our approach directly targets the underlying failure mechanism, pore-pressure and matric suction evolution, providing a continuous assessment of slope stability across the full hydrological continuum, from dry unsaturated conditions to complete saturation. Several studies have demonstrated that unsaturated soil mechanics can significantly influence slope stability, particularly in steep terrain where negative pore pressures increase effective stress and therefore shear resistance (Fredlund and Rahardjo, 1993; Lu and Likos, 2004; Lepore et al., 2013; Lu and Godt, 2008). In this context, the framework presented here extends previous approaches by explicitly incorporating the soil-water retention

https://doi.org/10.5194/egusphere-2026-1599
Preprint. Discussion started: 4 May 2026

relationship into the inverted stability formulation, allowing the identification of instability thresholds under both saturated and unsaturated conditions.

Our methodology generates spatially distributed maps of critical hydrological states (Fig. 6), effectively creating a potential hazard activation map based on site-dependent hydrological and mechanical properties. Application to the Pontaiba basin in the Carnic Alps showed the delineation of the three distinct stability regimes: unconditionally stable terrain, CWI-controlled conditionally stable areas, and steep slopes where instability is governed by soil moisture dynamics, i.e. CSM-controlled. The emergence of a slope-dependent transition between groundwater-dominated and moisture-controlled instability provides an explanation for shallow landslide initiation in steep terrain under unsaturated conditions. This perspective aligns with the consensus that effective landslide hazard assessment must explicitly account for transient hydrological triggers rather than rainfall forcing alone.

The CSM and CWI metrics offer operational advantages for Early Warning Systems (EWS) because they are directly comparable with measurable or model-forecasted hydrological variables, such as soil moisture and groundwater levels. Compared with empirical rainfall threshold approaches commonly adopted in operational landslide EWSs (Guzzetti et al., 2008; Bogaard and Greco, 2018; Segoni et al., 2018), the proposed CWI–CSM framework shifts the focus from rainfall forcing to the hydrological state of the hillslope. This distinction is important because rainfall thresholds may vary significantly across climatic and geomorphological settings, while hydrological thresholds such as soil moisture or groundwater levels represent more direct proxies of slope stability conditions. Similar perspectives have recently emerged in studies that integrate soil moisture observations or hydrological modeling into landslide forecasting (Ponziani et al., 2012; Halter et al., 2025). The present framework contributes to this line of research by providing spatially distributed, physically interpretable hydrological thresholds that can potentially be linked to real-time monitoring or hydrological simulations, thereby strengthening the mechanistic basis of landslide hazard assessment.

A key advancement for EWS is the potential to reduce false alarms (Piciullo et al., 2018; Segoni et al., 2018a). Rainfall-threshold approaches often achieve high hit rates but at the cost of frequent false alerts, limiting their operational applicability (Nocentini et al., 2024) (Nocentini et al., 2024). In line with Rosi et al., (2021), our methodology would reduce false alarms by incorporating additional hydrological information, by distinguishing areas that require near-saturation (CWI-controlled) from those that are vulnerable under partial saturation (CSM-controlled). In steep terrain, the nonlinear decline of CSM with increasing slope implies that relatively small moisture increases may suffice to drive slopes toward instability, highlighting the importance of monitoring unsaturated zone dynamics during short-duration, high-intensity rainfall events. In regions such as the Carnic Alps, where precipitation extremes and complex glacial and colluvial deposits contribute to widespread landslide activity in the region (Palladino et al., 2018; Tunini et al., 2024) embedding these spatially explicit thresholds into operational systems could substantially enhance spatial warning precision.

Uncertainty of key soil-mechanical parameters is an issue in the spatial distributed approach (Arnone et al., 2016). The proposed framework explores parameter uncertainty through multiple scenario realizations of key geotechnical parameters. By evaluating model performance across a range of cohesion values and failure depths, the analysis identifies parameter

https://doi.org/10.5194/egusphere-2026-1599
Preprint. Discussion started: 4 May 2026

combinations that best reproduce observed landslide occurrence. This multi-scenario calibration yields a physically plausible optimal cohesion parameter and confirms the robustness of the approach at the basin scale. By linking instability thresholds to hydrological state variables rather than empirical rainfall statistics, the CWI-CSM framework focuses on the hillslope response controlling failure initiation. In practice, these thresholds can be evaluated when soil moisture or groundwater conditions are available from field monitoring or hydrological model simulations driven by rainfall inputs, providing a physically interpretable basis for assessing slope stability under varying hydrological conditions.

Several limitations must be acknowledged. First are the simplifying assumptions of the slope stability model, which assumes that the slope is laterally infinite and planar, neglecting three-dimensional effects and lateral stress redistribution (Iverson, 2000; Montgomery and Dietrich, 1994). Real hillslopes often present curvature, irregular geometry, and variable thickness of soil, which may significantly affect slope stability. The model is appropriate only for shallow translational landslides where the failure surface is approximately parallel to the ground surface and it is no suitable for other mechanics (Fredlund and Rahardjo, 1993). Model performance and sensitivity analyses further highlight the influence of uncertainties in geotechnical parameters and failure depth. Future research should therefore prioritize coupling the stability framework with distributed, process-based hydrological models to simulate transient responses, validating predictions against instrumented slopes, and incorporating additional processes such as vegetation effects and dynamic root cohesion.

In conclusion, the primary outcome of this work is a transferable methodology that converts topographic and soil information into maps of critical hydrological thresholds. While parameter values are site-specific, the analytical structure of the framework, linking slope stability to critical hydrological response thresholds, is transferable to other soil-mantled mountainous regions. These maps identify hydrologically sensitive terrain and provide a dynamic, physics-based alternative to static susceptibility mapping. Addressing the identified limitations will further enhance the physical realism and operational applicability of the proposed framework. Ultimately, the CSM and CWI metrics offer a direct and mechanistic basis for enhancing landslide early warning systems, a capability that is particularly relevant in mountainous regions subject to increasing precipitation extremes, where robust, process-based hazard assessment frameworks are essential for effective risk management.

Code, data, or code and data availability

The data and code used in this study are available from the authors upon reasonable request. Interested readers may obtain access by contacting the authors via email at elisa.arnone@uniud.it and thomasjuby@outlook.com.

Supplement link

The link to the supplement will be included by Copernicus, if applicable.

https://doi.org/10.5194/egusphere-2026-1599
Preprint. Discussion started: 4 May 2026

Author contributions

EA designed the methodology and the experiments. JT developed the methodology, the algorithms and performed the simulations. LVN and RLB reviewed the methodology and the experiments. JT prepared the first draft of the manuscript. EA, LVN and RLB revised the manuscript.

Competing interests

The authors declare that they have no conflict of interest.

Financial support

This research received funding from European Union NextGenerationEU – National Recovery and Resilience Plan (PNRR), Mission 4, Component 2, Investiment 1.1 -PRIN 2022 – 2022ZC2522 - CUP G53D23001400006. Prof. Bras was supported by the National Science Foundation, Geosciences, grant 2224973 and by the K. Harrison Brown Family Chair

References

Arnone, E., Noto, L. V., Lepore, C., and Bras, R. L.: Physically-based and distributed approach to analyze rainfall-triggered landslides at watershed scale, Geomorphology, 133, 121–131, https://doi.org/10.1016/j.geomorph.2011.03.019, 2011.

Arnone, E., Caracciolo, D., Noto, L. V., Preti, F., and Bras, R. L.: Modeling the hydrological and mechanical effect of roots on shallow landslides, Water Resour. Res., 52, 8590–8612, https://doi.org/10.1002/2015WR018227, 2016.

Arnone, E., Francipane, A., Dialynas, Y. G., Noto, L. V., and Bras, R. L.: Implications of terrain resolution on modeling rainfall-triggered landslides using a TIN- based model, Environmental Modelling & Software, 141, 105067, https://doi.org/10.1016/j.envsoft.2021.105067, 2021.

Arnone, E., Zoratti, V., Formetta, G., Bosa, S., and Petti, M.: Predicting peakflows in mountain river basins and data-scarce areas: a case study in northeastern Italy, Hydrological Sciences Journal, 68, 432–447, https://doi.org/10.1080/02626667.2022.2162408, 2023.

Arnone, E., Treppiedi, D., and Noto, L. V.: Analysis of high-resolution rain records in FVG, northeastern Italy, Proceedings of IAHS, 385, 5–10, https://doi.org/10.5194/piahs-385-5-2024, 2024.

Van Asch, Th. W. J., Buma, J., and Van Beek, L. P. H.: A view on some hydrological triggering systems in landslides, Geomorphology, 30, 25–32, https://doi.org/10.1016/S0169-555X(99)00042-2, 1999.

Bao, C. G., Gong, B., and Zhan, L.: Properties of unsaturated soils and slope stability of expansive soils, in: Keynote Lecture, Proceedings of the 2nd International Conference on Unsaturated Soils (UNSAT 98). Beijing, China, 71–98, 1998.

https://doi.org/10.5194/egusphere-2026-1599
Preprint. Discussion started: 4 May 2026

Baum, R. L., Godt, J. W., and Savage, W. Z.: Estimating the timing and location of shallow rainfall-induced landslides using a model for transient, unsaturated infiltration, J. Geophys. Res. Earth Surf., 115, https://doi.org/10.1029/2009JF001321, 2010.

Bishop, A. W.: The use of the Slip Circle in the Stability Analysis of Slopes, Géotechnique, 5, 7–17, https://doi.org/10.1680/geot.1955.5.1.7, 1955.

Bogaard, T. and Greco, R.: Invited perspectives: Hydrological perspectives on precipitation intensity-duration thresholds for landslide initiation: proposing hydro-meteorological thresholds, Natural Hazards and Earth System Sciences, 18, 31–39, https://doi.org/10.5194/nhess-18-31-2018, 2018.

Brilli, N., Masi, E. B., Rossi, G., and Tofani, V.: Slope stability modelling of shallow landslides at a regional scale, Geoenvironmental Disasters, 12, 18, https://doi.org/10.1186/s40677-025-00323-x, 2025.

Brunetti, M. T., Gariano, S. L., Melillo, M., Rossi, M., and Peruccacci, S.: An enhanced rainfall-induced landslide catalogue in Italy, Sci. Data, 12, 216, https://doi.org/10.1038/s41597-025-04551-6, 2025.

Cucchiaro, S., Martini, L., Maset, E., Pellegrini, G., Eliana Poli, M., Beinat, A., Cazorzi, F., and Picco, L.: Multi-temporal analysis to support the management of torrent control structures, Catena (Amst)., 235, 107599, https://doi.org/10.1016/j.catena.2023.107599, 2024.

DiBiagio, A., Capobianco, V., Oen, A., and Tallaksen, L. M.: State-of-the-art: parametrization of hydrological and mechanical reinforcement effects of vegetation in slope stability models for shallow landslides, Landslides, 21, 2417–2446, https://doi.org/10.1007/s10346-024-02300-1, 2024.

Dietrich, W. E., Reiss, R., Hsu, M., and Montgomery, D. R.: A process-based model for colluvial soil depth and shallow landsliding using digital elevation data, Hydrol. Process., 9, 383–400, https://doi.org/10.1002/hyp.3360090311, 1995.

Emberson, R., Kirschbaum, D., and Stanley, T.: New global characterisation of landslide exposure, Natural Hazards and Earth System Sciences, 20, 3413–3424, https://doi.org/10.5194/nhess-20-3413-2020, 2020.

Estermann, R., Rajczak, J., Velasquez, P., Lorenz, R., and Schär, C.: Projections of Heavy Precipitation Characteristics Over the Greater Alpine Region Using a Kilometer–Scale Climate Model Ensemble, Journal of Geophysical Research: Atmospheres, 130, https://doi.org/10.1029/2024JD040901, 2025.

Del Fabbro, M., Paronuzzi, P., and Bolla, A.: Geotechnical Characterisation of Flysch-Derived Colluvial Soils from a Pre-Alpine Slope Affected by Recurrent Landslides, Geosciences (Basel)., 14, 115, https://doi.org/10.3390/geosciences14050115, 2024.

FAO: Harmonized World Soil Database version 2.0, FAO; International Institute for Applied Systems Analysis (IIASA);, https://doi.org/10.4060/cc3823en, 2023.

Fratianni, S. and Acquaotta, F.: The Climate of Italy, 29–38, https://doi.org/10.1007/978-3-319-26194-2_4, 2017.

Fredlund, D. G., Xing, A., Fredlund, M. D., and Barbour, S. L.: The relationship of the unsaturated soil shear strength to the soil-water characteristic curve, Canadian Geotechnical Journal, 33, 440–448, https://doi.org/10.1139/t96-065, 1996.

Fredlund, D. G. . and Rahardjo, H. .: Soil mechanics for unsaturated soils, Wiley, 517 pp., 1993.

https://doi.org/10.5194/egusphere-2026-1599
Preprint. Discussion started: 4 May 2026

Fredlund, D. G. ., Rahardjo, H. ., and Fredlund, M. D. .: Unsaturated soil mechanics in engineering practice, John Wiley & Sons, 2012.

Froude, M. J. and Petley, D. N.: Global fatal landslide occurrence from 2004 to 2016, Natural Hazards and Earth System Sciences, 18, 2161–2181, https://doi.org/10.5194/nhess-18-2161-2018, 2018.

van Genuchten, M. Th.: A Closed-form Equation for Predicting the Hydraulic Conductivity of Unsaturated Soils, Soil Science Society of America Journal, 44, 892–898, https://doi.org/10.2136/sssaj1980.03615995004400050002x, 1980.

Gobiet, A., Kotlarski, S., Beniston, M., Heinrich, G., Rajczak, J., and Stoffel, M.: 21st century climate change in the European Alps—A review, Science of The Total Environment, 493, 1138–1151, https://doi.org/10.1016/j.scitotenv.2013.07.050, 2014.

Guzzetti, F., Peruccacci, S., Rossi, M., and Stark, C. P.: The rainfall intensity–duration control of shallow landslides and debris flows: an update, Landslides, 5, 3–17, https://doi.org/10.1007/s10346-007-0112-1, 2008.

Hengl, T., Mendes de Jesus, J., Heuvelink, G. B. M., Ruiperez Gonzalez, M., Kilibarda, M., Blagotić, A., Shangguan, W., Wright, M. N., Geng, X., Bauer-Marschallinger, B., Guevara, M. A., Vargas, R., MacMillan, R. A., Batjes, N. H., Leenaars, J. G. B., Ribeiro, E., Wheeler, I., Mantel, S., and Kempen, B.: SoilGrids250m: Global gridded soil information based on machine learning, PLoS One, 12, e0169748, https://doi.org/10.1371/journal.pone.0169748, 2017.

Iverson, R. M.: Landslide triggering by rain infiltration, Water Resour. Res., 36, 1897–1910, https://doi.org/10.1029/2000WR900090, 2000.

Khalili, N. and Khabbaz, M. H.: A unique relationship for χ for the determination of the shear strength of unsaturated soils, Géotechnique, 52, 76–77, https://doi.org/10.1680/geot.52.1.76.40832, 2002.

Lepore, C., Arnone, E., Noto, L. V., Sivandran, G., and Bras, R. L.: Physically based modeling of rainfall-triggered landslides: a case study in the Luquillo forest, Puerto Rico, Hydrol. Earth Syst. Sci., 17, 3371–3387, https://doi.org/10.5194/hess-17-3371-2013, 2013.

Lu, N. and Godt, J.: Infinite slope stability under steady unsaturated seepage conditions, Water Resour. Res., 44, https://doi.org/10.1029/2008WR006976, 2008.

Lu, Ning. and Likos, W. J. .: Unsaturated soil mechanics, John Wiley & Sons, Inc., 556 pp., 2004.

Ménégoz, M., Valla, E., Jourdain, N. C., Blanchet, J., Beaumet, J., Wilhelm, B., Gallée, H., Fettweis, X., Morin, S., and Anquetin, S.: Contrasting seasonal changes in total and intense precipitation in the European Alps from 1903 to 2010, Hydrol. Earth Syst. Sci., 24, 5355–5377, https://doi.org/10.5194/hess-24-5355-2020, 2020.

Montgomery, D. R. and Dietrich, W. E.: A physically based model for the topographic control on shallow landsliding, Water Resour. Res., 30, 1153–1171, https://doi.org/https://doi.org/10.1029/93WR02979, 1994.

Nocentini, N., Medici, C., Barbadori, F., Gatto, A., Franceschini, R., del Soldato, M., Rosi, A., and Segoni, S.: Optimization of rainfall thresholds for landslide early warning through false alarm reduction and a multi-source validation, Landslides, 21, 557–571, https://doi.org/10.1007/s10346-023-02176-7, 2024.

Öberg, A. and Sällfors, G.: Determination of Shear Strength Parameters of Unsaturated Silts and Sands Based on the Water Retention Curve, Geotechnical Testing Journal, 20, 40–48, https://doi.org/10.1520/GTJ11419J, 1997.

https://doi.org/10.5194/egusphere-2026-1599
Preprint. Discussion started: 4 May 2026

Palladino, M. R., Viero, A., Turconi, L., Brunetti, M. T., Peruccacci, S., Melillo, M., Luino, F., Deganutti, A. M., and Guzzetti, F.: Rainfall thresholds for the activation of shallow landslides in the Italian Alps: the role of environmental conditioning factors, Geomorphology, 303, 53–67, https://doi.org/10.1016/j.geomorph.2017.11.009, 2018.

Peruccacci, S., Gariano, S. L., Melillo, M., Solimano, M., Guzzetti, F., and Brunetti, M. T.: The ITAlian rainfall-induced LandslIdes CAtalogue, an extensive and accurate spatio-temporal catalogue of rainfall-induced landslides in Italy, Earth Syst. Sci. Data, 15, 2863–2877, https://doi.org/10.5194/essd-15-2863-2023, 2023.

Piciullo, L., Calvello, M., and Cepeda, J. M.: Territorial early warning systems for rainfall-induced landslides, Earth. Sci. Rev., 179, 228–247, https://doi.org/10.1016/j.earscirev.2018.02.013, 2018.

Ponziani, F., Pandolfo, C., Stelluti, M., Berni, N., Brocca, L., and Moramarco, T.: Assessment of rainfall thresholds and soil moisture modeling for operational hydrogeological risk prevention in the Umbria region (central Italy), Landslides, 9, 229–237, https://doi.org/10.1007/s10346-011-0287-3, 2012.

Ramos-Scharrón, C. E., Arima, E. Y., and Hughes, K. S.: An assessment of the spatial distribution of shallow landslides induced by Hurricane María in Puerto Rico, Phys. Geogr., 43, 163–191, https://doi.org/10.1080/02723646.2020.1801121, 2022.

Reichenbach, P., Rossi, M., Malamud, B. D., Mihir, M., and Guzzetti, F.: A review of statistically-based landslide susceptibility models, Earth. Sci. Rev., 180, 60–91, https://doi.org/10.1016/j.earscirev.2018.03.001, 2018.

Roman Quintero, D. C., Marino, P., Abdullah, A., Santonastaso, G. F., and Greco, R.: Large-scale assessment of rainfall-induced landslide hazard based on hydrometeorological information: application to Partenio Massif (Italy), Natural Hazards and Earth System Sciences, 25, 2679–2698, https://doi.org/10.5194/nhess-25-2679-2025, 2025.

Rosi, A., Segoni, S., Canavesi, V., Monni, A., Gallucci, A., and Casagli, N.: Definition of 3D rainfall thresholds to increase operative landslide early warning system performances, Landslides, 18, 1045–1057, https://doi.org/10.1007/s10346-020-01523-2, 2021.

Schaap, M. G., Leij, F. J., and van Genuchten, M. Th.: rosetta : a computer program for estimating soil hydraulic parameters with hierarchical pedotransfer functions, J. Hydrol. (Amst)., 251, 163–176, https://doi.org/10.1016/S0022-1694(01)00466-8, 2001.

Schaap, M. G., Nemes, A., and van Genuchten, M. Th.: Comparison of Models for Indirect Estimation of Water Retention and Available Water in Surface Soils, Vadose Zone Journal, 3, 1455–1463, https://doi.org/10.2136/vzj2004.1455, 2004.

Segoni, S., Piciullo, L., and Gariano, S. L.: A review of the recent literature on rainfall thresholds for landslide occurrence, Landslides, 15, 1483–1501, https://doi.org/10.1007/s10346-018-0966-4, 2018a.

Segoni, S., Piciullo, L., and Gariano, S. L.: Preface: Landslide early warning systems: monitoring systems, rainfall thresholds, warning models, performance evaluation and risk perception, Natural Hazards and Earth System Sciences, 18, 3179–3186, https://doi.org/10.5194/nhess-18-3179-2018, 2018b.

Sidle, R. C. and Bogaard, T. A.: Dynamic earth system and ecological controls of rainfall-initiated landslides, Earth. Sci. Rev., 159, 275–291, https://doi.org/10.1016/j.earscirev.2016.05.013, 2016.

https://doi.org/10.5194/egusphere-2026-1599
Preprint. Discussion started: 4 May 2026

Sodemann, H. and Zubler, E.: Seasonal and inter-annual variability of the moisture sources for Alpine precipitation during 1995–2002, International Journal of Climatology, 30, 947–961, https://doi.org/10.1002/joc.1932, 2010.

Tarolli, P. and Dalla Fontana, G.: Hillslope-to-valley transition morphology: New opportunities from high resolution DTMs, Geomorphology, 113, 47–56, https://doi.org/10.1016/j.geomorph.2009.02.006, 2009.

Taylor, D. W.: Fundamentals of Soil Mechanics, John Wiley & Sons, New York, 1948.

Terzaghi, K.: Theoretical soil mechanics, John Wiley & Sons, New York, 1943.

Terzaghi, K., Peck, R. B., and Mesri, G.: Soil Mechanics in Engineering Practice, 3rd ed., John Wiley & Sons, New York, 1996.

Trigila, A., Iadanza, C., Romeo, S., Di Paola, G., Gambino, P., Calcaterra, S., Zastrow, L. R., Romano, D., Biondo, T., Noman, M., Di Muro, F., and Dragoni, A.: Advancing landslide knowledge and dissemination in Italy through IdroGEO 2.0 web platform, Landslides, 23, 477–487, https://doi.org/10.1007/s10346-025-02592-x, 2026.

Tsai, T.-L. and Yang, J.-C.: Modeling of rainfall-triggered shallow landslide, Environmental Geology, 50, 525–534, https://doi.org/10.1007/s00254-006-0229-x, 2006.

Tunini, L., Zuliani, D., Di Traglia, F., Borselli, L., De Luca, C., Nolesini, T., and Casu, F.: Monitoring and modelling moraine landslides: an example from Cazzaso village (Carnic Alps, Italy), Bulletin of Geophysics and Oceanography, 65, 327–346, 2024.

Vanapalli, S. K. and Fredlund, D. G.: Comparison of Different Procedures to Predict Unsaturated Soil Shear Strength, in: Advances in Unsaturated Geotechnics, 195–209, https://doi.org/10.1061/40510(287)13, 2000.

Vanapalli, S. K., Fredlund, D. G., Pufahl, D. E., and Clifton, A. W.: Model for the prediction of shear strength with respect to soil suction, Canadian Geotechnical Journal, 33, 379–392, https://doi.org/10.1139/t96-060, 1996.

van Westen, C. J., van Asch, T. W. J., and Soeters, R.: Landslide hazard and risk zonation—why is it still so difficult?, Bulletin of Engineering Geology and the Environment, 65, 167–184, https://doi.org/10.1007/s10064-005-0023-0, 2006.

Wu, W. and Sidle, R. C.: A Distributed Slope Stability Model for Steep Forested Basins, Water Resour. Res., 31, 2097–2110, https://doi.org/10.1029/95WR01136, 1995.

Youden, W. J.: Index for rating diagnostic tests, Cancer, 3, 32–35, https://doi.org/10.1002/1097-0142(1950)3:1<32::AID-CNCR2820030106>3.0.CO;2-3, 1950.

Zhang, Y. and Schaap, M. G.: Weighted recalibration of the Rosetta pedotransfer model with improved estimates of hydraulic parameter distributions and summary statistics (Rosetta3), J. Hydrol. (Amst)., 547, 39–53, https://doi.org/10.1016/j.jhydrol.2017.01.004, 2017.